Analysis of On-Board Hazard Detection and Avoidance for Safe Lunar Landing

Andrew E. Johnson, Andres Huertas, Robert A. Werner and James F. Montgomery
aej@jpl.nasa.gov, ahuertas@jpl.nasa.gov, rawerner@jpl.nasa.gov, monty@jpl.nsa.gov
Jet Propulsion Laboratory, California Institute of Technology
Pasadena, CA 91109

Abstract—Landing hazard detection and avoidance technology is being pursued within NASA to improve landing safety and increase access to sites of interest on the lunar surface. The performance of a hazard detection and avoidance system depends on properties of the terrain, sensor performance, algorithm design, vehicle characteristics and the overall all guidance navigation and control architecture. This paper analyzes the size of the region that must be imaged, sensor performance parameters and the impact of trajectory angle on hazard detection performance. The analysis shows that vehicle hazard tolerance is the driving parameter for hazard detection system design.

TABLE OF CONTENTS

1. Introduction 1
2. Hazard Detection and Avoidance Processing 2
3. Hazard Map Area Analysis 2
4. Hazard Detection Analysis 5
5. Trajectory Angle Analysis 6
6. Discussion 7
7. Conclusion 8
Acknowledgment 8
References 8
Biographies 8

1. INTRODUCTION

Landing hazards are surface features that could damage or tip the lander over during touch down. Landing hazards include tall rocks, steep slopes, scarps, cliffs and craters. The purpose of Hazard Detection and Avoidance (HDA) is to autonomously detect these hazards (hazard detection) near the landing site and then determine a new landing site that is free of hazards (safe site selection). Landing hazards exist everywhere on the Moon and many of the more desirable landing sites are near the most hazardous terrain (e.g., the rim of Shackleton Crater), so HDA is needed to autonomously and safely land payloads over much of the lunar surface. The HDA requirements used in the Autonomous Landing and Hazard Avoidance Technology (ALHAT) Project are to detect hazards that are more than 0.3 m tall and slopes that are greater than 5 degrees. In addition to detecting these hazards, the HDA capability must also be able to find a safe landing site free of these hazards for a lunar lander with diameter ~15m over most of the lunar surface.

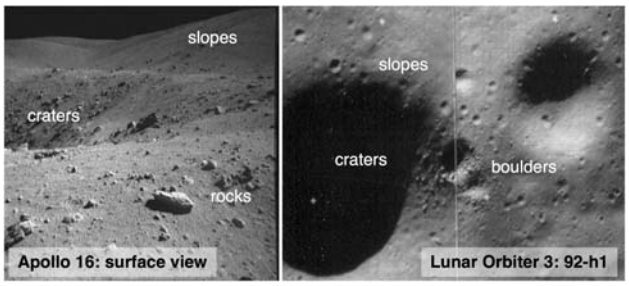

Figure 1: Example lunar landing hazards.

Imaging LIDAR (light detection and ranging) sensors are ideal sensors for on-board hazard detections because they can generate direct measurements of the lunar surface elevation from high altitude. This paper describes a suite of analyses that have been conducted to determine the working requirements for lidar-based HDA in the ALHAT project. These include high fidelity Monte Carlo simulations to determine the required ground spacing between lidar samples (ground sample distance) and the noise on the lidar range measurement. This high fidelity simulation has also been used to determine the effect of viewing on hazard detection performance. Another analysis has investigated the probability of the existence of a hazard free landing site as a function of lander diameter, hazard map area and rock coverage. Together these analyses have determined a set of working requirements for HDA that are being used to guide sensor development and the overall Guidance Navigation and Control architecture.

1-4244-1488-1/08/$25.00 ©2008 IEEE.
IEEEAC paper #1656, Version 2, Updated December 14th, 2008

2. HAZARD DETECTION AND AVOIDANCE PROCESSING

HDA algorithms for landing on the Moon and Mars have been proposed for both passive visible [8][9][10] and lidar sensors [7]. Our lidar-based approach to HDA combines targeted lidar data collection with an efficient hazard detection algorithm [6].

Hazard Digital Elevation Map Construction

The Hazard Digital Elevation Map (HDEM) is an elevation map created from lidar data in a region that contains the nominal landing site. The HDEM must be large enough to contain at least one safe landing site (analysis in Section 3.), and it must have high enough resolution and low enough noise for hazard detection (analysis in Section 4.). During landing, the lidar is commanded to collect range data that covers the HDEM at the required resolution. Calibration data is used to convert the lidar range and angle data to Cartesian (x, y, z) 3D points in the lidar sensor frame. These points are then transformed into a local level coordinate frame using position and attitude data provided by the GN&C system. For each 3D point, the bin in the HDEM that the point falls in is determined and then bilinear interpolation of point elevation is used to deal with the uneven sampling of the surface by the lidar data. The left side of Figure 2 shows the steps in HDEM construction.

Hazard Detection and Safe Site Selection.

Steep slopes, rocks, cliffs and gullies are all hazards for landing. By computing the local slope and roughness in an elevation map, all of these hazards can be detected. We use the algorithm described in [6] to measure slope and roughness hazards. The algorithm proceeds as follows. First the HDEM is partitioned into square regions the size of the lander footprint so that local slopes can be computed efficiently on the length scale set by the lander. In each region a robust plane is fit to the DEM data using least median squares. A smooth underlying elevation map is generated by bi-linearly interpolating the elevation of the robust planes at the center of each region. A local roughness map is then computed as the absolute difference between HDEM elevations and this smooth underlying terrain map. Slope is defined as the angle between the local surface normal and the gravity vector; each robust plane has a single slope. A slope map is generated by bi-linearly interpolating the robust plane slope from the center of each region.

The lander will have thresholds on the maximum slope and maximum roughness that can be handled by the mechanical landing system. Selection of the safe site starts by generating binary images from the slope and roughness maps; parts of the maps that are above the threshold (hazards) are positive while parts that are below are zero (not a hazard). The roughness and slope hazards are grown by the diameter of the lander using a grassfire transform [2] applied to each map. The logical-OR of the grown slope and roughness hazard maps creates the safe landing map. The center of Figure 2 shows examples of slope, roughness and hazard maps with green to yellow to red color maps; red is above threshold and green is well below threshold.

A grassfire transform is applied to the safe landing map to generate a Distance To Nearest Hazard (DTNH) cost function for the remaining safe landing area. The point that has greatest distance is selected as the best landing site. If there are multiple bins with the same distance from hazards then the one closest to the a-priori landing site is selected. The area around the selected safe site is set to zero in the DTNH map and a new safe site that has the maximum distance in the new DTNH map is selected. This masking and selection process proceeds until the DNTH map is free of non-zero distances. The sites selected in this manner are then passed in selected order to the GN&C system, which will combine them with fuel consumption and other constraints in order to select the best safe site at a system level for landing.

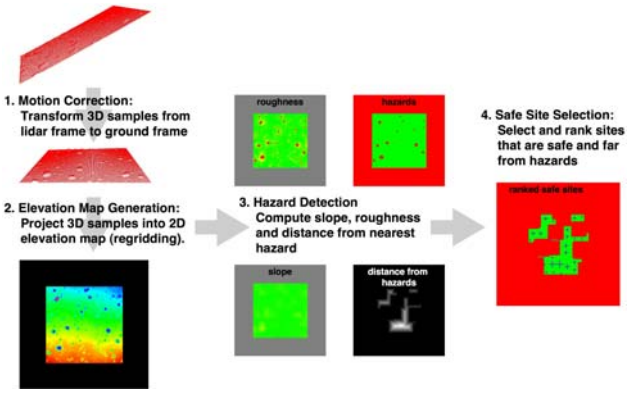

Figure 2: Hazard detection processing steps.

3. HAZARD MAP AREA ANALYSIS

The Hazard Map Area (HMA) (i.e., the area covered by the HDEM) must be large enough that there is at least one hazard free landing zone in the HDEM. This assumes that there is only enough time and fuel to generate a single HDEM during descent. There is also a competing desire to make the HMA as small as possible to reduce the quantity of sensor data that must be collected and processed. Two major factors influence the HMA: the number hazards in the region and the size of the area under the lander that must be free of hazards. First we describe the parameters and models that influence the hazard map area, and then we describe the Monte Carlo analysis conducted to explore the sensitivity of the HMA to the parameters.

Rock Abundance

If hazard detection is perfect (all hazards are detected and there are no false positives), then the number of hazards in the region is a function of the vehicle hazard tolerance and the spatial distribution model of hazards. In this analysis we

have assumed that rocks are the only hazards; this assumption is a reasonable starting point because rocks are the primary hazards that cannot be identified and avoided through a-priori landing site selection. Future analysis will study crater and slope hazards using similar methods.

Rock distribution models describe the number of rocks per square meter as a function of a few parameters. Models have been developed for the moon [9] and Mars [3]. The Golombek and Rapp model describes the cumulative fractional area covered by rocks F with an the exponential form

$$F(k,D) = ke^{-q(k)D}$$
$$q(k) = a + b/k \tag{1}$$

where k is the total fractional area covered by rocks (i.e., the abundance), D is rock diameter and a and b are constants set based on data. In contrast, the Shoemaker and Morris model is a power law for the number of rocks N per unit area

$$N(k,\gamma,D) = kD^{\gamma} \tag{2}$$

where D is rock diameter and k and γ are coefficients fit to the data. In [3], Golombek and Rapp discuss the two models and conclude that the exponential model is more accurate because it produces less rocks at large diameters which is consistent with data from Mars landing sites and several rocky terrestrial sites. For this reason, we have chosen the Golombek and Rapp model for our analysis.

Figure 3 shows the Golombek and Rapp model for difference rock abundances after Equation 1 has been converted to the cumulative number of rocks per square meter. Figure 4 shows 3D renderings of synthetic terrain maps with difference rock abundances. Qualitatively, it can be seen that the number and size of the rocks increases with increasing rock abundance.

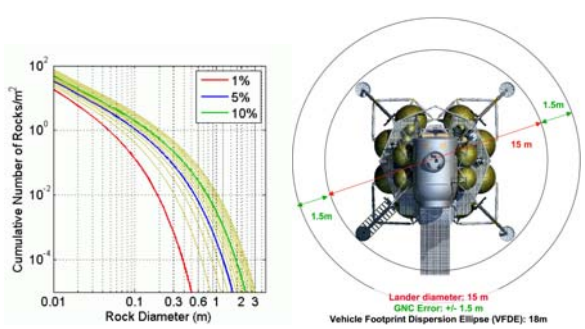

Figure 3: Exponential rock density model (left) and definition of the Vehicle Footprint Dispersion Ellipse (VFDE).

At this time, the rock abundance for possible landing sites on the moon is unknown. To get a feel for the range of rock abundances on the moon, we fit the rock data from the Surveyor landings [4] to the exponential rock model. The resulting rock abundances varied from 3% to 17%. Studies of areas near craters on Mars [3] indicate that rock abundance can be as high as 40% at the edge of a fresh crater. It seems unlikely that future lunar landers will be targeted to such regions, so in the required HMA was assessed abundances between 2% and 20%.

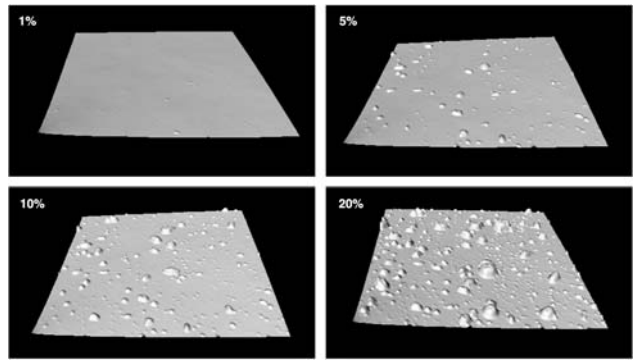

Figure 4: Examples of rocky terrain maps with 1% to 20% rock area coverage over 25m x 25m patches.

Vehicle Hazard Tolerance

The other parameter that drives the number of hazards in the hazard map is the hazard tolerance of the vehicle. After significant research, we have not found a specification for the rock hazard tolerance of the Apollo lunar lander, and a requirement on the rock tolerance of the next generation lunar lander has not been specified. Given this dearth of information, the hazard tolerance was kept as a free parameter in the HMA analysis that varied from 0.3 m to 0.6m.

Vehicle Footprint Dispersion Ellipse

The safe site must be large enough to contain the lander footprint. Since the vehicle will accumulate guidance navigation and control errors after the hazards are detected, the safe site must also be large enough to account for these errors. The term Vehicle Dispersion Footprint Ellipse (VFDE) has been coined to describe the area that combines the size of the vehicle and these GN&C errors. Figure 3 shows an example 18m diameter VFDE for the lunar lander vehicle (15m diameter) and +/-1.5m of GN&C errors. In the HMA analysis, the VFDE was varied from 16m to 24m.

Analysis

Figure 5 shows the qualitative impact of changing the rock abundance and the VFDE. The plots show a 90m x 90m Hazard Map (HMA = 8100 m^2). The small dots indicate hazardous rocks that have been synthetically generated as follows. Using the exponential model the number of rocks per square meter as a function of diameter is computed (c.f., Figure 3). This function is scaled by 8100 m^2 to obtain the number of rocks at each diameter in the Hazard Map. The rocks with heights greater than the hazard tolerance of the vehicle are then distributed randomly across the map using a uniform spatial distribution. The green circles in the plots indicate hazard

free VFDEs.

For the 5% abundance and 16m VFDE there are numerous places to land. If the VFDE is increased to 20m, the number of places to land decreases slightly. However if the VFDE is changed back to 16m, but the abundance is increased to 10%, then the number of safe sites decreases dramatically (only one site really). If the VFDE is then increased to 20m, there are no places to land at all.

A Monte Carlo analysis was conducted using the approach used to generate Figure 5. The Monte Carlo parameters were HMA (45x45m^2, 90x90m^2, 180x180m^2, 360x360m^2), rock abundance (2%, 4%,…,20%), VFDE (16m,18m,…,24m) and hazard tolerance (30cm, 40cm, 50cm, 60cm). For each parameter instance (HMA, abundance, VFDE, tolerance), 500 maps populated with hazards were generated. Each map was assessed to see if at least one safe site appeared in the map; the ensemble of maps produced a statistic on the probability of at least one safe site appearing for that parameter instance. This process was repeated for all of the parameter instances to assess the sensitivity to each parameter. It should be emphasized that this analysis assumed perfect hazard detection and that the only hazards present are rocks.

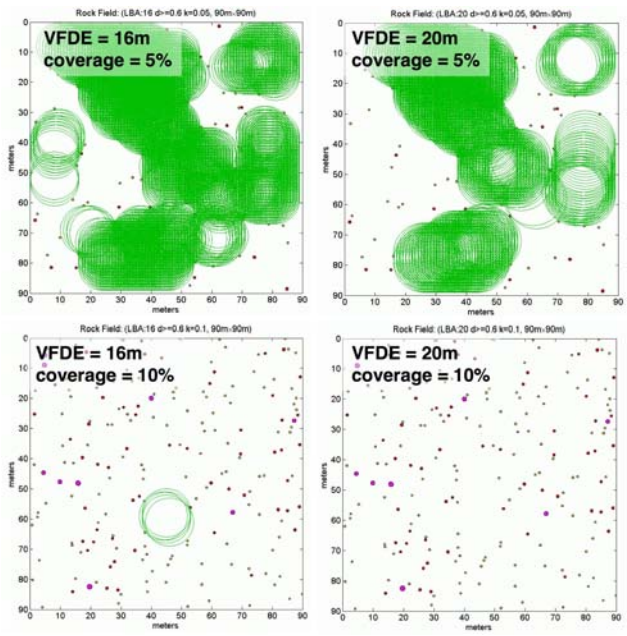

Figure 5: The effect of Vehicle Footprint Dispersion Ellipse (VFDE) and rock abundance on the number of safe sites in a 90m x 90m Hazard Map Area (HMA) assuming a 30cm rock hazard tolerance.

Figure 6 shows four plots for the different HMA and a hazard tolerance of 30cm. Only 2% to 10% rock abundance results are shown because higher abundances are very difficult to land in with a 30cm tolerance. For a 2% rock abundance there is always a safe place to land in areas greater than 45x45m^2. However as abundance increases the probability of a safe site decreases rapidly. As the VFDE increases the probability of a safe site appears to decrease linearly; as the HMA increases by powers of 2, the probability of a safe site grows somewhat linearly.

Figure 7 shows four plots for the different HMA and a hazard tolerance of 50cm. For clarity, only the larger rock abundances (12% to 20%) are shown. There is a dramatic increase in the probability of at least one safe site when compared to the plots in Figure 6. For example for a 90m x 90m HMA and a rock abundance of 10%, the probability of finding a safe site is around 10%; with a tolerance of 50cm and a rock abundance of 20%, this probability increases to nearly 100%. This is a significant improvement in landing safety achieved by just making the hazard tolerance 20cm higher. This sensitivity is due to the fact that the number of hazardous rocks drops off exponentially as hazard tolerance is increased linearly.

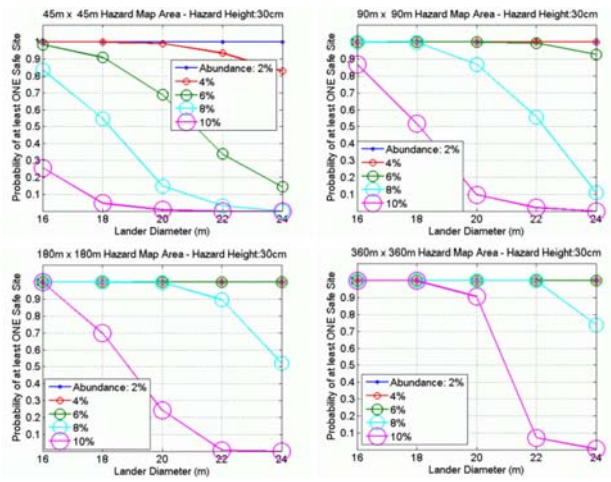

Figure 6: Hazard Map Area analysis for a 30cm hazard tolerance.

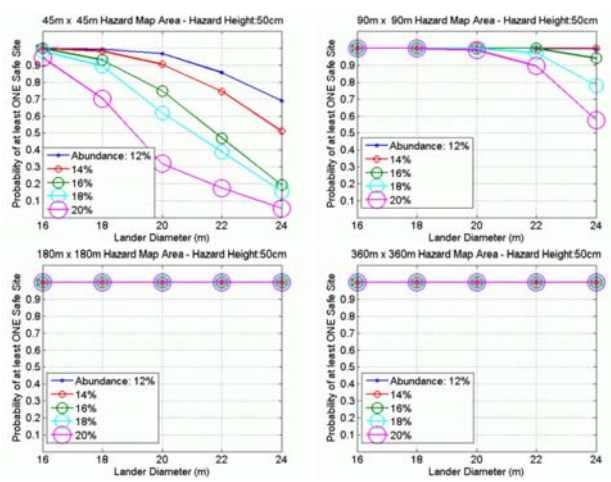

Figure 7: Hazard Map Area analysis for a 50cm hazard tolerance.

The plots in Figure 5 and Figure 6 can be used during lander design to inform system level choices. For example, if it known that the targeted landing site has a 10% rock coverage and the lander has a hazard tolerance of 30cm,

then the VFDE must be less than 18m for a 360m x 360m HMA or less than 16m for a 180m x 180m HMA. Either choice leads to an HDA system that can image a large area and also have small GN&C position errors after hazard detection. In contrast, if the hazard tolerance is increased to 50cm, then even with an abundance of 12% the HMA can be decreased to 45x45m and a VFDE less than 20m or a 90m x 90m HMA and a VFDE of 24m. Either case is much easier to implement than the 30cm tolerance cases.

4. HAZARD DETECTION ANALYSIS

Hazard detection and avoidance operates on the HDEM, an elevation map built up from lidar range measurements that covers the hazard map area. The performance of hazard detection is driven by the horizontal post separation of the HDEM and the random noise on the elevation for each posting. From a algorithm viewpoint there is a desire to make these parameters as small as possible to maximize hazard detection performance. From the sensor viewpoint there is a desire to make them as large as possible to reduce sensor performance requirements (e.g., IFOV, timing resolution).

Parameters

The HDA algorithm sets the resolution of elevation map such that the post separation is matched to the nominal spacing of the lidar samples on the ground (i.e., the *ground sample distance (GSD)*). Since this construction approach associates (on average) one lidar sample with each elevation post, the noise on the elevation is close to the noise on the range measurement from the lidar (σ_R).

Figure 8 shows how these parameters influence hazard detection. The figure shows two hemispherical rocks: one is below the vehicle hazard tolerance (safe) and one is above (hazard). The lidar measurements are shown as red dots. If the lidar GSD is too large, then there will not be enough samples on the hazard rock to detect it. σ_R is represented by the purple ellipses. If σ_R is too large then it is possible that a hazardous rock may not be detected (bottom of left ellipse) and it is also possible that a safe rock will be detected as a hazard, which is a false positive (right ellipse). This analysis seeks to find values for GSD and σ_R that are just small enough to provide adequate detection performance.

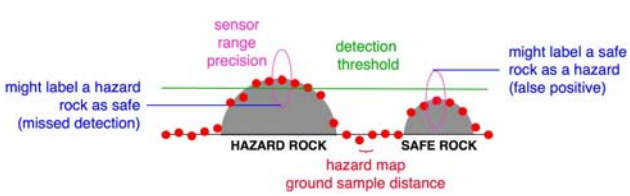

Figure 8: Hazard detection parameters.

High Fidelity HDA Simulation

A high fidelity simulation was used to assess hazard detection. This simulation consists of terrain maps, a high fidelity lidar simulator and the HDA algorithm described in Section 2. .

To expedite analysis the terrain maps used were very simple. Each terrain map consisted of two hemispherical shaped rocks: one rock above and one rock below the vehicle hazard tolerance. Because the position of the rocks relative to the lidar samples effects hazard detection performance, the rocks were randomly placed within a 10m-diameter disk with at least 4m between rocks. Hemispherical rocks were used because this shape is simple to analyze and follows the model that rocks are typically half buried. By adjusting the rock heights the effect of changing vehicle hazard tolerance on GSD and σ_R can be assessed. In the analysis, the hazard rock height was set to the vehicle hazard tolerance to assess the performance for detecting the smallest hazard. The safe rock was set to half the height of the hazard rock height and the detection threshold was set to the midpoint between these two heights. These height heuristics are adequate for this analysis, but will need to change when assessing hazard detection for a field of hazards that follow the exponential distribution model.

The high fidelity lidar simulator used has been described previously [6]. Essentially, it simulates a scanning LIDAR in motion above a surface represented by a digital terrain map. For each laser pulse, the ranging model simulates that intersection of the pulse with the terrain (by modeling the pulse as multiple rays emanating from the sensor) and applies representative return detection logic to simulate the range measurement performance. Applying this ranging model over a field of regard generates scans or range images. The scanning pattern is parameterized so that arbitrary fields of view and resolutions can be generated. The lidar model is where the GSD and σ_R are adjusted.

ALHAT team members at Johnson Space Center provided a typical descent trajectory for lunar landing. This trajectory was used to generate the motion of the LIDAR during data collection. Data collection lasted 1 second and started when the vehicle was at 500m altitude; the lidar parameters were set such that the specified GSD and σ_R were obtained at 500m. The lidar field of view was fixed so that it covered the 10m rocks disk that contained the safe and hazard rocks. The HDA algorithm took the lidar data and motion corrected it using perfect knowledge of the trajectory. The HDEM was constructed and hazard detection was performed. The hazard detection results were then compared to the real position of the safe and hazard rocks to assess detection.

Analysis

Monte Carlo analysis using the high fidelity simulator was conducted over a spread of vehicle hazard tolerances, GSD and σ_R. The vehicle hazard tolerance was varied from 0.3 to 1.0 m in steps of 0.1m. The GSD was varied from 0.1

to 0.4 m in steps of 0.1m. σ_R was varied from 0.25m to 0.10 m (one sigma). For each parameter triple 100 Monte Carlo runs were performed. Between runs the position of the rocks moved around in the field of view of the lidar and the random seed on the range error changed. The hazard detection results from the 100 runs were used to generate the statistics on:

- percent true positives (TP) = number of times the hazard rock was detected / number of runs
- false positive rate (FP) = number of detections not on hazard rock / number of runs
- false positive area (FPA) = area (m^2) covered by false positives

If there are a significant number of false positives, they will begin to overlap in the hazard map. Because false positives are counted as disjoint regions in the hazard map, this will cause the false positive rate to decrease even though the area that is identified as hazardous is increasing. For this reason the false positive area is used as a performance metric.

Figure 9 contains two tables that show the results for a 30cm hazard tolerance and a 50cm hazard tolerance. The green, yellow and red shading gives quick visual indication of the performance; green boxes correspond to TP>=95, FP<1 and FPA<1; yellow boxes correspond to 90 <TP < 95, 1<FP<2, and 1<FPA<2; red boxes correspond to TP<90, FP>2 and FPA>2.

To obtain perfect detection of a 30cm hazard, the GSD should be less than 10cm and σ_R<0.025cm. To obtain perfect detection of a 50cm hazard, the GSD should be less than 30cm and σ_R<0.05cm. In each case the GSD and σ_R can be increased with a slight decrease in detection performance and increase in false positives.

Hazard Rock= 0.3 m
Safe Rock = 0.15 m

Range Measurement Sigma		Cross Track Sample Spacing 0.4m	0.3m	0.2m	0.1m
0.025m	% true positives	22	44	97	100
	false positive rate	0	0	0	0
	false positive area	0	0	0	0
0.050m	% true positives	24	46	95	100
	false positive rate	0	0	0.1	1.2
	false positive area	0	0	0	0.07
0.075m	% true positives	22	54	93	100
	false positive rate	1.1	2.3	7.3	29.6
	false positive area	0	0.02	0.3	2.06
0.100m	% true positives	27	57	91	100
	false positive rate	15.9	27.6	73.2	258
	false positive area	0.45	0.69	2.72	8.87

Hazard Rock= 0.5 m
Safe Rock = 0.25 m

Range Measurement Sigma		Cross Track Sample Spacing 0.4m	0.3m	0.2m	0.1m
0.025m	% true positives	90	100	100	100
	false positive rate	0	0	0	0
	false positive area	0	0	0	0
0.050m	% true positives	85	100	100	100
	false positive rate	0	0	0	0
	false positive area	0	0	0	0
0.075m	% true positives	84	99	100	100
	false positive rate	0.1	0.1	0.1	0.6
	false positive area	0	0	0	0
0.100m	% true positives	77	95	100	100
	false positive rate	0.2	0.2	0.8	5.5
	false positive area	0	0	0.04	0.53

Figure 9: Hazard detection performance.

These results agree with expectation. Due to the hemispherical shape of the hazards more than one sample across the hazard is required; the results indicate 4 to 6 samples are required. Also to prevent false positives on the safe rock from appearing, the range measurement noise needs to be small compared to the separation between the hazard detection threshold and the safe rock. The tables indicate that the separation is between 3 and 5 times σ_R.

5. TRAJECTORY ANGLE ANALYSIS

The final analysis was to determine the effect of trajectory angle on hazard detection performance. Apollo used a trajectory that was 16˚ from horizontal. Although this may be better for human landing and the Apollo illumination conditions, angles near the horizon are very challenging for sensor-based hazard detection. As shown in Figure 10, when the LIDAR is pointed nadir toward the ground all of the lidar samples are spaced an equal distance apart in both horizontal directions and there are no shadows. As the trajectory angle decreases the samples are stretched in the viewing direction. This results in shadows on the far sides of hazards and effectively increases the GSD by the sine of the trajectory angle. If the look angle is close to horizontal then cracks will appear in the terrain map where there are no sensor data which will cause false positives; this effect can be eliminated by increasing the GSD of the sensor, but this will decrease hazard detection performance. Possibly the worst effect from near horizontal trajectory angles is that the top of the rock hazards will be foreshortened. This will reduce the probability that the top of the rock will be detected and will consequently reduce the probability of hazard detection.

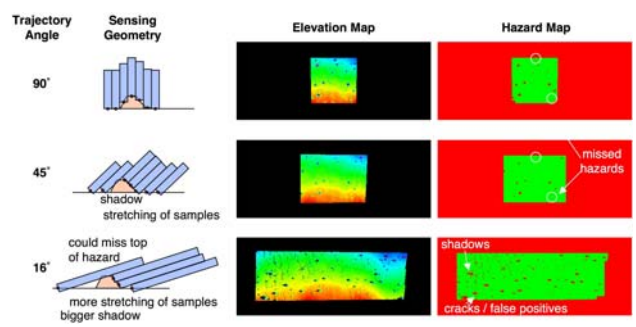

Figure 10: Effect of trajectory angle on hazard detection.

Parameters

The high fidelity simulation infrastructure was used to obtain a quantitative assessment of the effect of trajectory angle. In this analysis, the trajectory used during lidar data collection was varied. Four trajectories were used corresponding to trajectory angle from horizontal of 16˚, 45˚, 60˚ and 90˚. The same simple terrain maps containing two rocks were used with hazard rocks of 30cm or 50cm. The scanning lidar model was used to generate synthetic lidar data, and the lidar parameters were set so that the

divergence of the laser was 0.2mrad, which corresponds to a 0.2m GSD at 1000m altitude and a 90˚ trajectory angle. For this analysis the lidar range measurement noise and pointing errors were turned off. For each trajectory lidar data was acquired at multiple slant ranges (500m, 750m, 1000m, 1500m and 2000m) and the HDA algorithm was applied to detect hazards.

For each hazard rock height, trajectory and slant range triple 100 Monte Carlo runs were performed. Between runs the position of the rocks moved around in the field of view of the LIDAR. The hazard detection results from the 100 runs were used to generate the statistics on percent true positives, false positive rate and false positive area.

Analysis

Figure 11 plots the detection rate for the 30cm hazard rock for the four trajectory angles and five slant ranges. The 90˚ trajectory angle (straight down) has the best performance as expected. There is perfect hazard detection up to 1000m slant range, which is consistent with the data in the top table of Figure 9 for a 0.2m GSD. Just decreasing the trajectory to 60˚ decreases the detection performance to an unacceptable level at 1000m and to recover detection performance the slant range must be decreased to 500m. The results are even worse for 45˚ and 16˚ trajectory angles. As discussed previously, the degraded performance is primarily due to an increasing GSD in the viewing direction.

Figure 12 shows a similar plot for the 50cm hazard. The performance has improved mainly because the sensor parameters are fixed and the hazard rock has gotten larger. The plot shows that a 50cm tall hazard can be detected reliably at 500m slant range and a 16˚ trajectory angle. At 45˚ the 50cm hazard can be reliably detected out to 1000m.

6. Discussion

The three separate analyses can be tied together to generate a set of consistent hazard detection parameters. Figure 13 and Figure 14 show parameter flow diagrams for possible hazard detection systems that are designed to detect 30cm and 50cm high hazards. These figures are two examples of possible HDA parameters; many other combinations exist. Each example assumes a 45˚ trajectory angle because that angle balances sensor performance against crew visibility constraints. They also hold to a 90m x 90m touch down area so that only a small divert is required to reach the safe landing site. The HDA data collection time is held to 3s for two reasons. Shorter times are easier to implement from a system perspective because the data collection system can be designed assuming that the data is collected at nearly the same altitude. It also forces the data to be available quickly so that the pilot can get real time feedback on hazard locations. It also allows for multiple HDA data collections to occur during a single landing (although the parameters are set so that only one is needed). Current designs for the next generation lunar lander have landing diameters around 15m, so this parameter is also fixed for each example.

For a 30cm hazard parameters (Figure 13) the system is only capable of handling an 8% rock abundance and it must have a rather tight GNC touchdown position errors of +/- 1.5m. Achieving such a small touchdown error relative to hazards may require feature tracking or hazard relative navigation, which complicates system design. The hazard detection occurs at 500m slant range so there is not a significant amount of time to conduct hazard detection before landing. The GSD is only 0.1m which forces the IFOV/divergence of the LIDAR to be small (0.07mrad to account for the 45˚ trajectory angle) and also forces a high sample rate from the sensor (270 kHz). Many of these parameters may be hard to achieve in practice, which makes HDA for 0.3m hazards quite challenging.

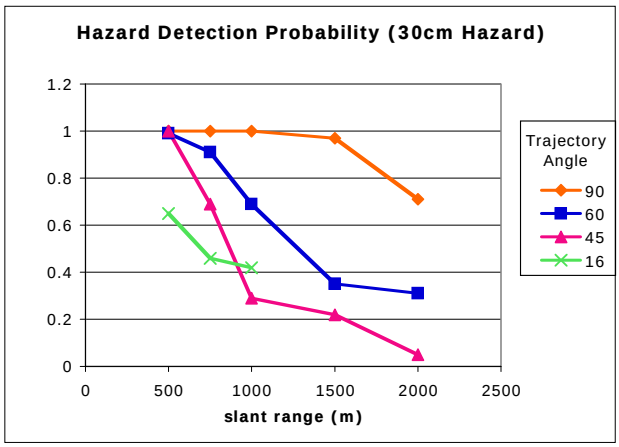

Figure 11: Percentage of true positive hazard detections as a function of slant range and trajectory angle for a 30cm high hazard rock.

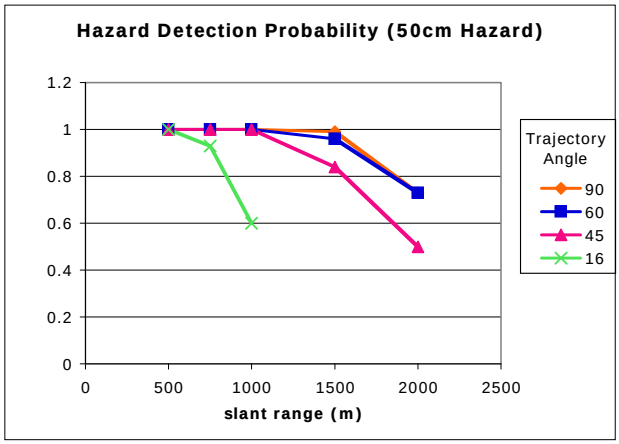

Figure 12: Percentage of true positive hazard detections as a function of slant range and trajectory angle for a 50cm high hazard rock.

Somewhat as expected, the parameters for detecting 0.5m tall hazards are more relaxed relative to 0.3m hazards. Hazard detection can occur at 1000 m slant range which provides more time to perform HDA opening up the possibility of performing HDA multiple times to add robustness to the system. Since the GSD is 0.3m the sample rate is lower and the required divergence/IFOV is larger which will reduce requirements on the LIDAR sensor. The increased range precision also eases requirements in the LIDAR. The GNC Touchdown errors are +/- 2.5 meters, which may eliminate the need for feature tracking or hazard relative navigation. Even with the relaxation in many parameters values, the system is still capable of landing in a 20% rock abundance, which should cover most feasible lunar landing sites.

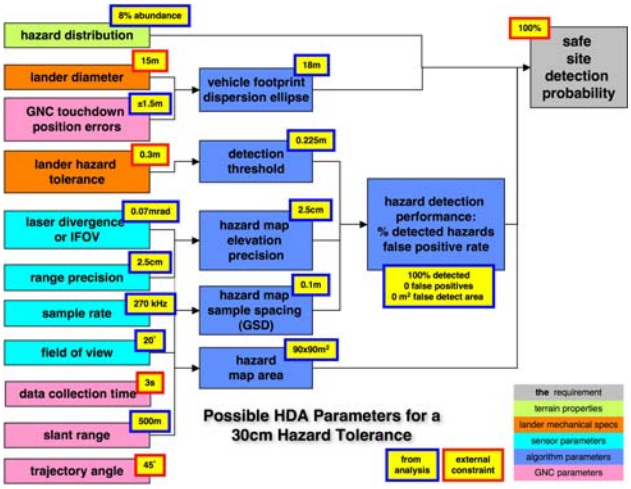

Figure 13: Possible hazard detection performance parameters for a 30cm vehicle hazard tolerance.

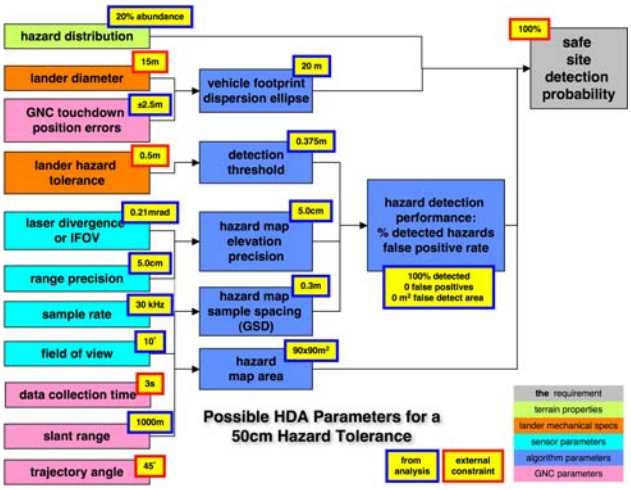

Figure 14: Possible hazard detection performance parameters for a 50cm vehicle hazard tolerance.

7. CONCLUSION

This paper has shown that many different parameters must be considered when designing a hazard detection and avoidance system. Due to the exponential form of rock distribution models the single most important parameter is the rock hazard tolerance of the lander vehicle. Increasing the hazard tolerance dramatically decreases the number of landing hazards and also decreases the area that has to be imaged and the number of samples across the image. This in turn makes it easier to implement the sensor system that provides the elevation data.

ACKNOWLEDGMENT

The work described in this publication was performed at the Jet Propulsion Laboratory, California Institute of Technology, under contract from the National Aeronautics and Space Administration. The authors would like to thank Ron Sostaric at JSC for providing the trajectory data.

REFERENCES

[1] D. Bernard and M. Golombek, "Crater and rock hazard modeling for Mars landing," *Proc. Space 2001 Conference and Exposition*, 2001

[2] H. Blum, "Biological Shape and Visual Science," *J. Theoretical Biology*, **38**, pp. 205-287, 1973.

[3] M. Golombek and D. Rapp, "Size Frequency Distribution of Rocks on Mars and Earth Analog Sites; Implications for Future landed Missions," *Jour. Geophysical Research*, **102**(E2), pp. 4117-4129, 1997.

[4] https://www.lpi.usra.edu/wiki/lunaref/index.php/Rock_Distributions_on_the_Lunar_Surface, 2007.

[5] R. Hutton and A. Evenson, *Lunar Surface Models*, NASA SP-8023, 55pp. 1969.

[6] A. Johnson, A. Klumpp, J. Collier and A. Wolf, "Lidar-based Hazard Avoidance for Safe Landing on Mars," *AIAA Jour. Guidance, Control and Dynamics*, **25**(5), 2002.

[7] C. Langley et al., "Recent Advancements of the Lidar-Based Autonomous Planetary Landing System." *Proc. 58th, Int'l Astronautical Conference*, Paper #IAC-07-A52, September 2007.

[8] L. Matthies, A. Huertas, Y. Cheng and A. Johnson, " Landing Hazard Detection with Stereo Vision and Shadow Analysis," *Proc. AIAA Infotech at Aerospace Conference*, Paper # AIAA 2007-2835, 2007.

[9] R. T. Schappell and R. L. Knickerbocker, "Experimental and Simulation Study Results of an Adaptive Video Guidance System," *AIAA Journal of Spacecraft*, **13**(9), pp. 557-563, 1976.

[10] S. Strandmore, T. Jean-Marius, and S. Trinh, "Toward a Vision Based Autonomous Planetary Lander," *Proc. AIAA GN&C Conf.* Paper # AIAA-99-4154, 1999.

[11] E. M. Shoemaker and E. C. Morris, *Radio Science*, **5**(2), pp. 129-155, 1970.

BIOGRAPHIES

Dr. Andrew Johnson *is a Principal Member of Technical Staff in the Computer Vision Group at JPL. He is the terrain sensing algorithm lead for the Autonomus Landing and Hazard Avoidance Project which is developing technology for safe and precise landing for the next generation manned lunar lander. At JPL he works on development, validation and flight implementation of computer vision systems for planetary landers and Mars rovers. He was the lead algorithm developer for the Mars Exploration Rover*

Descent Image Motion Estimation System and is currently developing the rover Visual Odometry algorithm from the Mars Science Laboratory.

Andres Huertas *is a Senior Member of the Technical Staff at the Jet Propulsion Laboratory. He earned his B.S. degree in Systems and Computing Engineering from Universidad de los Andes in 1974, and his M.S. and Engineer degrees in Computer Science in 1978, and Electrical Engineering in 1984 from the University of Southern California. Prior to joining the Computer Vision Group at JPL in 2002, he worked on computer vision research since 1978 at the Image Processing Institute and at the Institute for Robotics and Intelligent Systems at the University of Southern California. At JPL, Andres works on computer vision techniques for autonomous off-road navigation, and on techniques for hazard detection for safe landing of spacecraft on planetary surfaces.*

QuickTime™ and a
TIFF (Uncompressed) decompressor
are needed to see this picture.

Dr. Robert Werner *obtained a Bachelor of Arts in Mathematics (1972) from the University of Iowa and a Master of Science in Engineering (1990) and Doctor of Philosophy (1996) from the University of Texas at Austin, both in aerospace engineering under a NASA Graduate Student Research Fellowship. Before attending graduate school, he worked at the University of Iowa's academic computer center (1970-1988) where he was ultimately titled Research and Development Project Leader. After graduate school he joined NASA's Jet Propulsion Laboratory (1996-present) where he has worked on autonomous navigation flight software ("AutoNav") for the Deep Space 1 and Deep Impact missions. Currently he is enhancing AutoNav, and working on the Autonomous Landing and Hazard Avoidance (ALHAT) project. His interests included computer graphics, operating systems, and microcomputers. Asteroid 3891 Werner is named in his honor.*

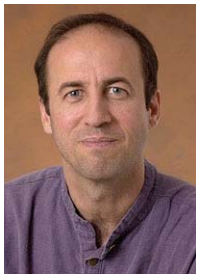

Dr. James Montgomery *is a Senior Member of Technical Staff at the Jet Propulsion Laboratory and is a member of the Guidance Navigation and Control Section. He has more than 15 years of experience in mobile robotics research and development and over 20 years of experience in software systems development for engineering applications, primarily in the fields of real-time embedded control, and signal and image processing. Since joining JPL, he has led the design, development and field testing of the JPL Autonomous Helicopter Testbed. He has also been involved in numerous technology development tasks for ground and aerial robots as well as planetary landing systems. He is currently the GN&C/EDL Field Test Lead for the Mars Science Laboratory Project.*